Electronic Supplementary Information for

Natural Organic Matter Adsorption Conditions Influence Photocatalytic Reaction Pathways of Phosphate-Treated Titanium Dioxide Nanoparticles

Riya A. Mathew,[1] Gang Wu,[2] Ye Zhang,[3,4] Sheyda Shakiba,[1] Yan Yao,[3,4] Ah-Lim Tsai,[2] and Stacey M. Louie[1*]

[1]Department of Civil and Environmental Engineering, University of Houston, Houston, TX 77004

[2]Department of Internal Medicine, McGovern Medical School, University of Texas Health Science Center at Houston, Houston, TX 77030

[3]Department of Electrical and Computer Engineering, University of Houston, Houston, TX 77004

[4]Texas Center for Superconductivity at the University of Houston, Houston, TX 77204

[*]Corresponding author:

Phone: 713-743-8646

Fax: 713-743-4260

Email: slouie@uh.edu

Pages: 22

Figures: 13

Tables: 1

Characterization of Suwannee River natural organic matter (NOM)

The Suwannee River NOM (2R101N) used throughout this study was purchased from the International Humic Substances Society, which reports the following characterization:

- Elemental composition, % (w/w), as determined on a dry, ash-free sample[1]:

  50.70 % C, 3.97 % H, 41.48 % O, 1.27 % N, and 1.78 % S

- Acidic functional group densities as estimated by titration[2]:

  11.21 meq $(g\ C)^{-1}$ carboxyl groups, and 2.47 meq $(g\ C)^{-1}$ phenolic groups

- Functional group composition as estimated by ^{13}C NMR[3]:

  8 % carbonyl, 20 % carboxyl, 23 % aromatic, 7 % acetal, 15 % heteroaliphatic, and 27 % aliphatic (note that these measurements are those reported for the 1R101N batch of Suwannee River NOM, as data were not available for the 2R101N batch)

Hydrodynamic size and zeta potential of TiO_2 nanoparticles (NPs)

Figure S1 presents the *z*-average and volume mean diameters for the initial stock suspensions and phosphate treated TiO_2 NPs by dynamic light scattering (DLS) (Figure S1a), the corresponding polydispersity index of the initial stock suspensions and phosphate treated TiO_2 NPs (Figure S1b), and the apparent zeta potentials for the TiO_2 upon overnight incubation in different water chemistries before ("unwashed") or after phosphate treatment (Figure S1c). All phosphate treated NPs were bath sonicated after washing in phosphate buffer, with uncoated NPs further probe sonicated to redisperse. Zeta potential was measured on 0.5 g L^{-1} TiO_2 NPs in a folded capillary zeta cell (DTS1070, Malvern Panalytical, Westborough, MA, USA) on a Malvern Zetasizer Nano ZS instrument with applied voltage of 150 V (automatic voltage selection). The Smoluchowski approximation was used to convert electrophoretic mobility to zeta potential.

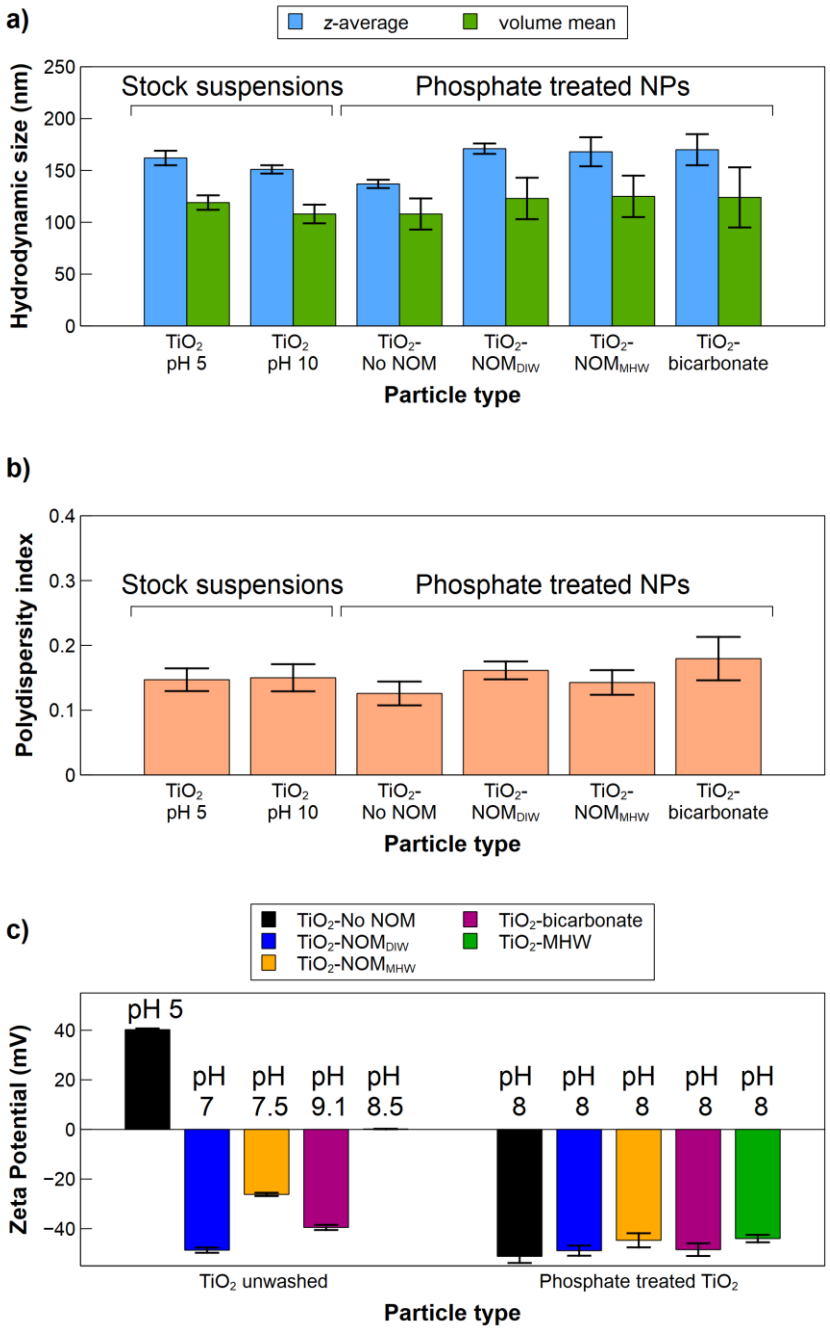

Figure S1. Hydrodynamic diameter (a) and polydispersity index (b) of TiO_2 stock suspensions and phosphate treated TiO_2 NPs measured on 0.1 g L^{-1} TiO_2 NPs; and apparent zeta potentials and measured pH of 0.5 g L^{-1} TiO_2 NPs before (unwashed) and after 10 mM phosphate washes (c).

Attenuated total reflectance – Fourier transform infrared (ATR-FTIR) analyses

ATR-FTIR spectra were first collected ("Experiment 1" described in the Methods in the main text) to evaluate *in situ* the adsorption of phosphate from 10 mM phosphate buffer (pH 8) after exposure to deionized water (DIW) (Figure S2). Also, in "Experiment 2," the adsorption of ions from moderately hard water (MHW) followed by adsorption of phosphate was tested (Figure S2). A strong phosphate peak[4] at 1077 cm^{-1} is observed in both cases, and the peak at 1395 cm^{-1} corresponds to bicarbonate ions from MHW. For the MHW, bicarbonate ions are first adsorbed, but are largely displaced upon phosphate washing. The spectra also did not show any observable peak at 1040 cm^{-1} that would be indicative of precipitation of hydroxyapatite species[5] when transferring from MHW to phosphate buffer.

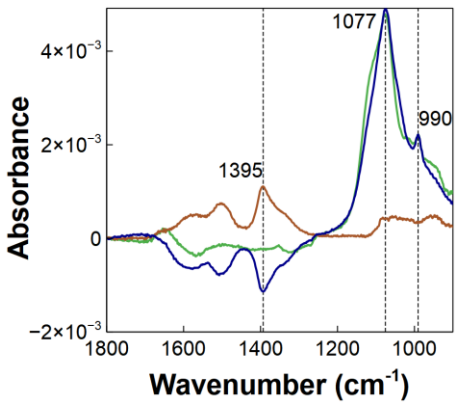

Figure S2. ATR-FTIR spectra of Experiment 1 for *in situ* adsorption of phosphate following exposure to DIW (green; background subtraction = TiO_2 in DIW); and Experiment 2 for ions from MHW adsorbing onto TiO_2 NPs (brown; background subtraction = TiO_2 in DIW), followed by phosphate exposure showing phosphate adsorption and bicarbonate displacement (blue; background subtraction = TiO_2 in MHW).

Control ATR-FTIR spectra were also collected to evaluate NOM functional groups and their interactions with the MHW without TiO_2 NPs. The deprotonated carboxylate (COO^-) groups of NOM typically produce moderately strong absorbances around 1580 cm^{-1} and 1400 cm^{-1} corresponding to asymmetrical and symmetrical stretching of the COO^-, and a shoulder around 1700 cm^{-1} for protonated COOH. Absorbances at ≈ 1100 cm^{-1} can be attributed to the C−O stretching vibration of ether groups.[6] For carboxylate species, comparison of the difference in asymmetrical and symmetrical frequencies ($\Delta\nu = \nu_{as} - \nu_s$) for the bound carboxylate relative to the free carboxylate ion has been reported to indicate binding or complexation modes. Specifically, for monodentate complexation, $\Delta\nu$ of the adsorbed carboxylate, $(\Delta\nu)_{adsorbed}$, will be higher than $\Delta\nu$ of the free ionic carboxylate, $(\Delta\nu)_{ionic}$; for bidentate chelating, $(\Delta\nu)_{adsorbed}$ will be lower than $(\Delta\nu)_{ionic}$; and for bidentate bridging, $(\Delta\nu)_{adsorbed}$ will be similar to $(\Delta\nu)_{ionic}$.[7, 8] To measure $(\Delta\nu)_{ionic}$ of the COO^-, either the NOM must be measured at a very high dissolved concentration to be able to obtain sufficient signal-to-noise of the NOM peaks above the background absorbance of the liquid water. Alternatively, here we dried the NOM from the supernatants of the centrifuged TiO_2 after coating with NOM in DIW at pH 7 (using NaOH for pH adjustment) to eliminate the liquid water interferences. The $(\Delta\nu)_{ionic}$ for the free NOM in DIW was (195 ± 1) cm^{-1} on duplicate measurements (representative spectrum in Figure S3a). The supernatant from the centrifuged TiO_2 after coating with NOM in MHW was also collected and washed twice with DIW using a 3 kDa filter to remove excess MHW salts, then dried for ATR-FTIR analysis. The $\Delta\nu$ for the free NOM in MHW was (174 ± 1) cm^{-1} on duplicate measurements (representative spectrum in Figure S3b). The lower $\Delta\nu$ in MHW is consistent with bidentate chelating of COO^- in the NOM with Ca^{2+}.

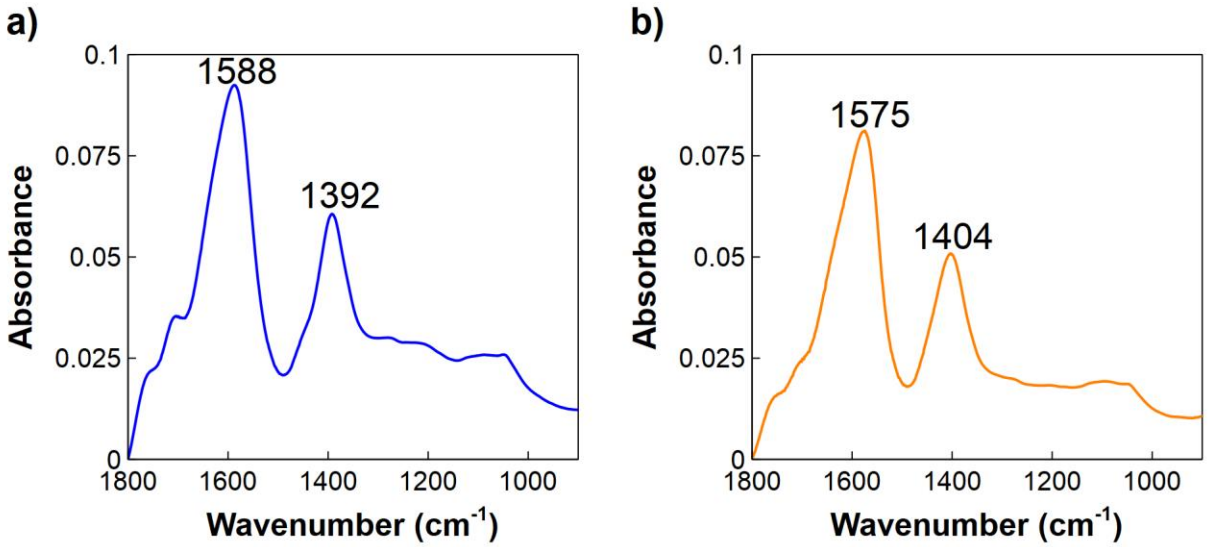

93

94 **Figure S3**. ATR-FTIR spectra of NOM_{DIW} without TiO_2 (collected as the supernatant after
95 adsorption to NPs in DIW) (a), and NOM_{MHW} without TiO_2 (collected as the supernatant after
96 adsorption to NPs in MHW followed by washing the NOM to remove excess salts) (b).

97

98 Finally, *in situ* experiments ("Experiments 3 and 4") were performed by depositing TiO_2,
99 equilibrating in the DIW or MHW background, introducing NOM in DIW or MHW until
100 adsorption was equilibrated, and finally followed by phosphate treatment. Both NOM adsorption
101 and phosphate adsorption and displacement of the NOM were monitored (Figure S4). Note in the
102 MHW, some displacement of HCO_3^- was observed upon NOM addition (identified as a small
103 negative peak at 1401 cm^{-1} overlaying the 1400 cm^{-1} NOM carboxylate peak, when subtracting
104 the initial MHW background from the final spectra collected after NOM adsorption, in Figure S4c,
105 black). This displacement occurred within the first 10 min of NOM exposure; subsequent spectra
106 of the NOM adsorption collected after the first spectrum showed only adsorption of the NOM
107 (Figure S4c, green). Jayalath et al.[6] reported that NOM likely coordinates with TiO_2 NPs by the
108 formation of inner sphere complexes, including monodentate (unidentate) and bidentate bridging

modes. For NOM adsorbed to TiO_2 in DIW, $(\Delta\nu)_{adsorbed}$ was 184 ± 2 cm^{-1} on triplicate measurements (Figure S4a), suggesting bidentate bridging given the similarity to $(\Delta\nu)_{ionic}$.[6] The lower $(\Delta\nu)_{adsorbed}$ for NOM adsorbed to TiO_2 in MHW was 170 ± 7 cm^{-1} on triplicate measurements (Figure S4c), indicative of bidentate chelating. However, given the similarity to $\Delta\nu$ for the NOM alone in MHW (Figure S3b), it is likely that the chelating is simply attributable to Ca^{2+} chelating onto the NOM itself and that the binding mode of NOM onto the TiO_2 (e.g. by Ca^{2+} bridging) is not identifiable in this case.

After phosphate treatment, spectra were processed by background subtracting either the original NOM-free background (red) to show remaining NOM and adsorbed phosphate, or by background subtracting the final adsorbed NOM layer to obtain a difference spectrum representing the NOM displacement (Figure S4b for DIW or S4d for MHW). Substantial displacement of the NOM was observed in both cases, along with phosphate peaks similar to those correspondingly observed in Figure S2. Although it can be possible to analyze peak losses semi-quantitatively (relative to the initial peak) using *in situ* experiments, for MHW, the displacement of bicarbonate that has overlapping peaks with the NOM makes these analyses challenging. Hence, size exclusion chromatography was used (as presented in the main text) for quantitative analyses and the ATR-FTIR spectra interpreted only qualitatively.

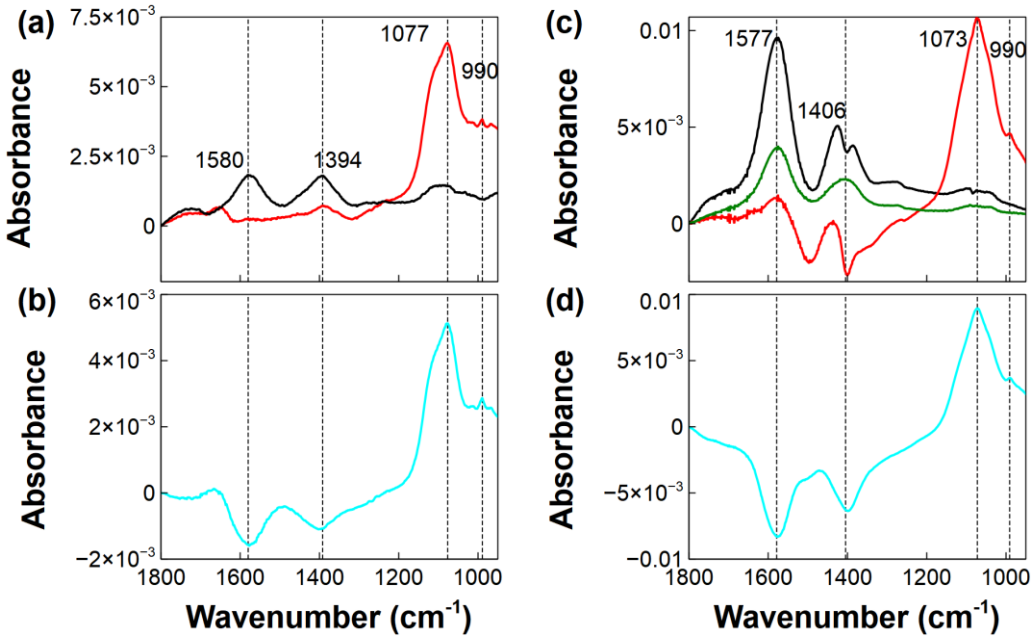

Figure S4. *In situ* ATR-FTIR spectra of NOM adsorbed from DIW to the TiO_2 NPs after 60 min adsorption (black), and the resulting surface chemistry (relative to DIW) after two 20-min washes in 10 mM phosphate buffer, pH 8 (red) (a). The spectra of the phosphate-treated NPs were also processed relative to the NOM adsorbed layer (black) to give the blue spectrum in (b) showing loss of NOM-related peaks. The corresponding analysis was also performed for NOM adsorption from MHW followed by desorption in phosphate buffer (c, d). Note the peak splitting in (c) is attributable to loss of bicarbonate; the green spectrum in (c) shows adsorption of NOM between 10 min and 60 min of NOM exposure to evaluate the NOM adsorption without interference from the bicarbonate desorption.

X-ray diffraction (XRD) analysis

To help verify the lack of precipitation of calcium phosphate salts during the exchange of the TiO_2 from MHW background to phosphate background, structural investigations of the TiO_2 samples were performed by using an X-ray powder diffractometer (MiniFlex600, Rigaku, Tokyo,

Japan) with Cu Kα1 radiation (λ = 1.5405 Å) in the angular range of 5−80° (2θ) with a step size of 0.02° and a scanning speed of 2° per minute. All samples were prepared by concentrating 15 mL of the 500 mg L^{-1} of phosphate treated TiO_2 NPs to 2 mL by centrifugation, followed by three washes into DIW and resuspending to 50 µL total volume after the final wash, then depositing by glass pipet onto a glass XRD slide and drying under a laminar flow hood. No significant differences between any of the TiO_2 samples and those prepared in DIW (with or without phosphate washing) were observed, indicating the lack of substantial precipitation of salts on the NPs (Figure S5).

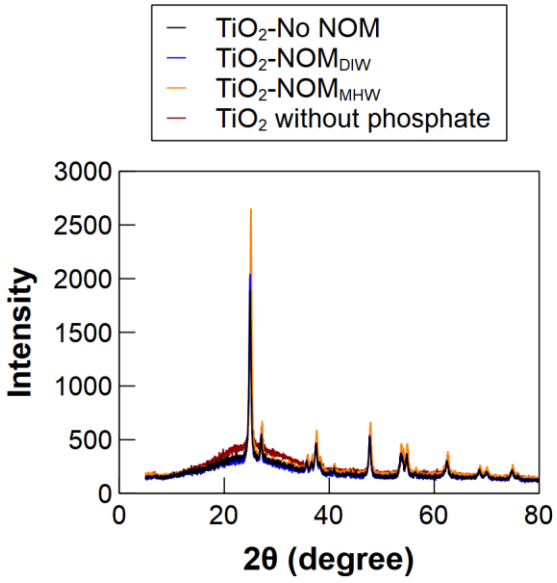

Figure S5. XRD spectra of TiO_2-No NOM, TiO_2-NOM_{DIW}, and TiO_2-NOM_{DIW} (all after phosphate treatment and washing into DIW to remove excess salts), and TiO_2 dried from DIW without phosphate for comparison.

Additional size exclusion chromatography (SEC) data

Supernatants were collected after equilibrating 500 mg L^{-1} of TiO_2 with 200 mg L^{-1} of NOM in DIW or MHW overnight and centrifuging, as well as after each of two washes into the phosphate buffer, and measured by SEC with both UV and dRI detection (raw chromatograms in Figure S6). The dRI is expected to provide more universally "equal" detection across all species (as opposed to UV extinction coefficients being variable across the sample), but a portion of the NOM coelutes with the dissolved gas or solvent peaks which produce interferences in the dRI signals.

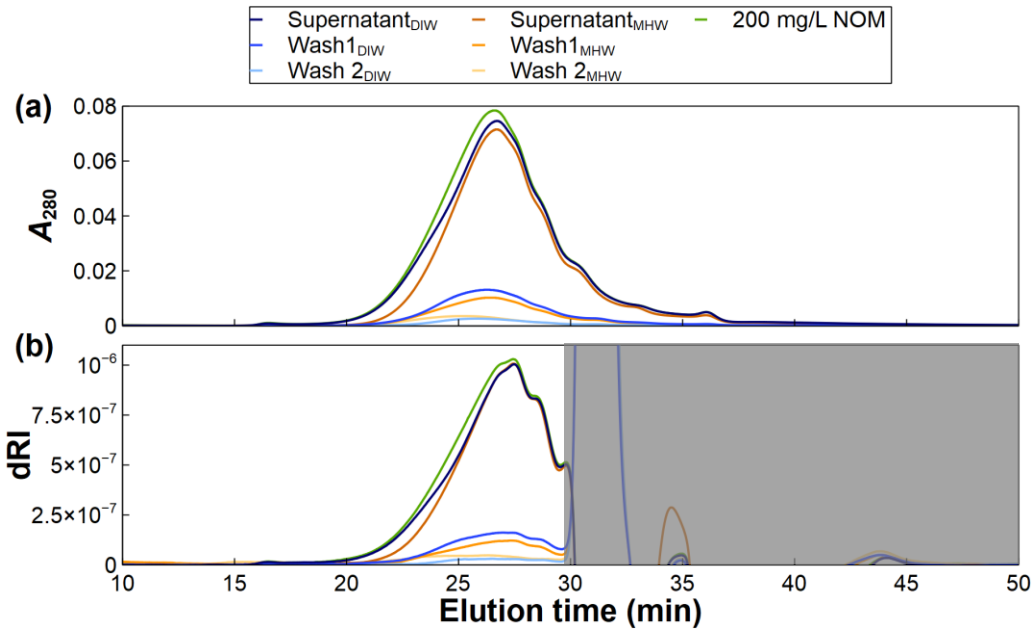

Figure S6. SEC-UV (a) and SEC-dRI (b) chromatograms of NOM remaining in solution from 200 mg L^{-1} of NOM after adsorbing to 500 mg L^{-1} of TiO_2 from DIW or MHW, as well as the NOM collected in the subsequent two washes into 10 mM phosphate buffer (pH 8) (a). The gray region indicates times during which the injected sample solvent or dissolved gases elute from the SEC column and hence dRI cannot be used to evaluate NOM.

To evaluate the initially adsorbed species, the initial "supernatant" SEC-UV chromatograms were subtracted from that of a control 200 mg L^{-1} NOM sample to produce the "TiO_2-NOM, Initial Adsorbed Layer" chromatograms in Figure 1 in the main text, while the difference in overall integrated UV peak areas for the supernatant and control was used to quantify the adsorbed mass. The NOM concentration in the supernatant ($C_{\text{supernatant}}$) is calculated assuming the concentration is proportional to the integrated SEC-UV peak area (A). Hence, given the UV peak area for a Suwannee River NOM control solution (A_{control}) with known concentration (C_{control}) (i.e., 200 mg L^{-1}), $C_{\text{supernatant}}$ can be computed from the measured peak area, $A_{\text{supernatant}}$ (eqn S1).

$$C_{\text{supernatant}} = \frac{A_{\text{supernatant}}}{A_{\text{control}}} C_{\text{control}} \quad \text{(S1)}$$

The initial NOM adsorbed is calculated as the difference in the NOM concentration in the control (i.e., 200 mg L^{-1}) and supernatants, i.e., $C_{\text{control}} - C_{\text{supernatant}}$. The subsequent wash into 10 mM phosphate buffer contains both NOM in the remaining supernatant from the previous stage, as well as NOM desorbed during the phosphate exposure. Hence, to determine *only* the newly desorbed species, a mass balance correction was made for the NOM remaining from the prior centrifugation stage:

$$A_{280,\text{desorbed in Wash 1}} = \frac{A_{280,\text{measured in Wash 1}} V_{\text{total}} - A_{280,\text{supernatant}} V_{\text{supernatant remaining}}}{V_{\text{total}}} \quad \text{(S2)}$$

where $V_{\text{supernatant remaining}}$ is the volume of remaining supernatant measured (gravimetrically) from the prior step, and V_{total} is the total volume when resuspending the NPs for Wash 1 (15 mL). Eqn S2 was used both on the integrated peak area to estimate the overall amount of NOM desorbed, and at each elution time point in the chromatograms to obtain the desorbed amount of each molecular weight fraction across the chromatogram. The desorbed mass could then be subtracted from the initially adsorbed mass to estimate the remaining adsorbed mass to give the "TiO_2-NOM, After 1st phosphate wash" chromatograms in Figure 1. Similarly, after Wash 2:

$$A_{280,\text{desorbed in Wash 2}} = \frac{A_{280,\text{measured in Wash 2}} V_{\text{total}} - A_{280,\text{measured in Wash 1}} V_{\text{Wash 1 remaining}}}{V_{\text{total}}} \quad \text{(S3)}$$

where $V_{\text{Wash 1 remaining}}$ is the volume of remaining Wash 1 liquid measured, and V_{total} is again the 15 mL total volume when resuspending the NPs for Wash 2. Subtracting the desorbed mass in Wash 2 gives the "TiO_2-NOM, Final adsorbed layer" in Figure 1 for the chromatographic analysis, and the final remaining adsorbed mass value reported in the main text for the integrated peak area analysis.

To estimate the molar masses of NOM across the distribution, the SEC was also coupled with an online multi-angle light scattering (MALS) detector to directly determine molar masses through a Zimm plot analysis, given the eluting concentration and by extrapolating MALS intensities across several scattering angles to zero angle. Details of this analysis are provided in our prior publications.[9-11] In brief, for calibration, a 2 g L^{-1} sample of bovine serum albumin (BSA) was injected and used for signal alignment, band broadening (i.e., dispersion), and MALS detector normalization. Then, 100 μL of a 3 g L^{-1} sample of Suwannee River NOM (pH 7) was injected to acquire sufficiently high MALS signals for the molar mass determination. The dRI detector was used as the concentration detector because it is presumed to be a more universal mass concentration detector than the UV detector with the refractive index increment, d*n*/d*c*, more consistent across the sample. However, the lower molar mass range cannot be analyzed as discussed above. The d*n*/d*c* was measured to be 0.146 mL g^{-1} (ref. 11) and was used to compute eluting mass concentrations from the measured dRI signal, and MALS data were analyzed across seven scattering angles selected for sufficient signal to noise for the data quality. The results are provided in Figure 1 in the main text, and the weight-average molar mass (26 kg mol^{-1}) determined here is similar to that reported in prior studies performing this analysis on Suwannee River NOM.[10, 12]

Quadrupole Time-of-Flight (QTOF) Mass Spectrometry to Affirm Degradation Byproducts

Liquid chromatography (LC) – QTOF mass spectra were collected on an Agilent 6545 QTOF in initial degradation experiments to affirm the identity of the major degradation byproducts before proceeding to the full set of experiments. The LC system and conditions were those reported in the main text. An atmospheric pressure chemical ionization (APCI) source was used for these phenolic compounds. First, the LC mobile phase composition (A: 0.01 % acetic acid in LC-MS water, B: methanol) was optimized on initial trials to maximize ionization efficiency and detector counts for phenol standards; then, the APCI source settings (temperatures, voltages, and corona current) were further optimized to the settings listed in Table S1 below.

Table S1. APCI Source Parameters

Polarity	Negative
Drying gas temperature	350 °C
Vaporizer temperature	350 °C
Drying gas flow	7 L min^{-1}
Nebulizer pressure	35 psi
Capillary voltage	2500 V
Corona current	4 μA
Fragmentor voltage	125 V
Skimmer	65V
Octopole 1 RF Vpp	750 V

The LC chromatograms for UV detection and total ion counts (TIC) are presented in Figure S7a for samples collected after 0 h and 1 h of UV exposure for bare TiO_2 with 20 mg L^{-1} initial phenol concentration. To acquire the mass spectra of the phenol and two major degradation byproducts, the QTOF was set to acquire scans from 40 to 1700 *m*/*z* and "All Ions" mode to

continuously cycle the collision cell between collision energies of 0, 10, 20, and 40 eV, with no precursor mass selection applied to the quadrupole. Continuous mass calibration was performed by introducing reference solution to monitor reference masses at *m*/*z* 119 and 980. The spectra of the unfragmented and fragmented compounds for phenol (from the 0 h sample, retention time 8 min) and hydroquinone and catechol byproducts (from the 1 h sample, retention time 1.7 and 3.8 min, respectively) are presented in Figure S7b. To mitigate the contribution of background ions to the spectra, a background spectrum was extracted either immediately prior or after the elution of the compound of interest and subtracted from the extracted spectrum across the compound peak.

Phenol shows the expected $[M\text{-}H]^-$ ion at *m*/*z* 93, as well as a fragment at *m*/*z* 65 consistent with loss of a CO group as has been reported previously.[13] The $[M\text{-}H]^-$ ion was also observed for catechol at *m*/*z* 109. However, both hydroquinone and catechol formed primarily ions with *m*/*z* 108 that would require formation of singly charged ions but loss of 2 H atoms. These ions have previously been reported to form for hydroquinone under APCI conditions and assigned to an $[M\text{-}2H]^{\bullet -}$ radical.[14] Because of the complexity of the ionization process, we did not assign further fragments and rather proceeded to validate the compound identification by purchasing known standards and verifying that the elution time and mass spectra matched those of the transformation products. It is also noted that ion formulas could be generated from the high-resolution mass spectra for other byproducts observed in the chromatogram, e.g. peaks eluting between the hydroquinone and catechol peaks, but identities could not be confirmed due to lack of available commercial standards. Hence, in all subsequent experiments, phenol, hydroquinone, and catechol were quantified by their UV peak areas against external calibration standards.

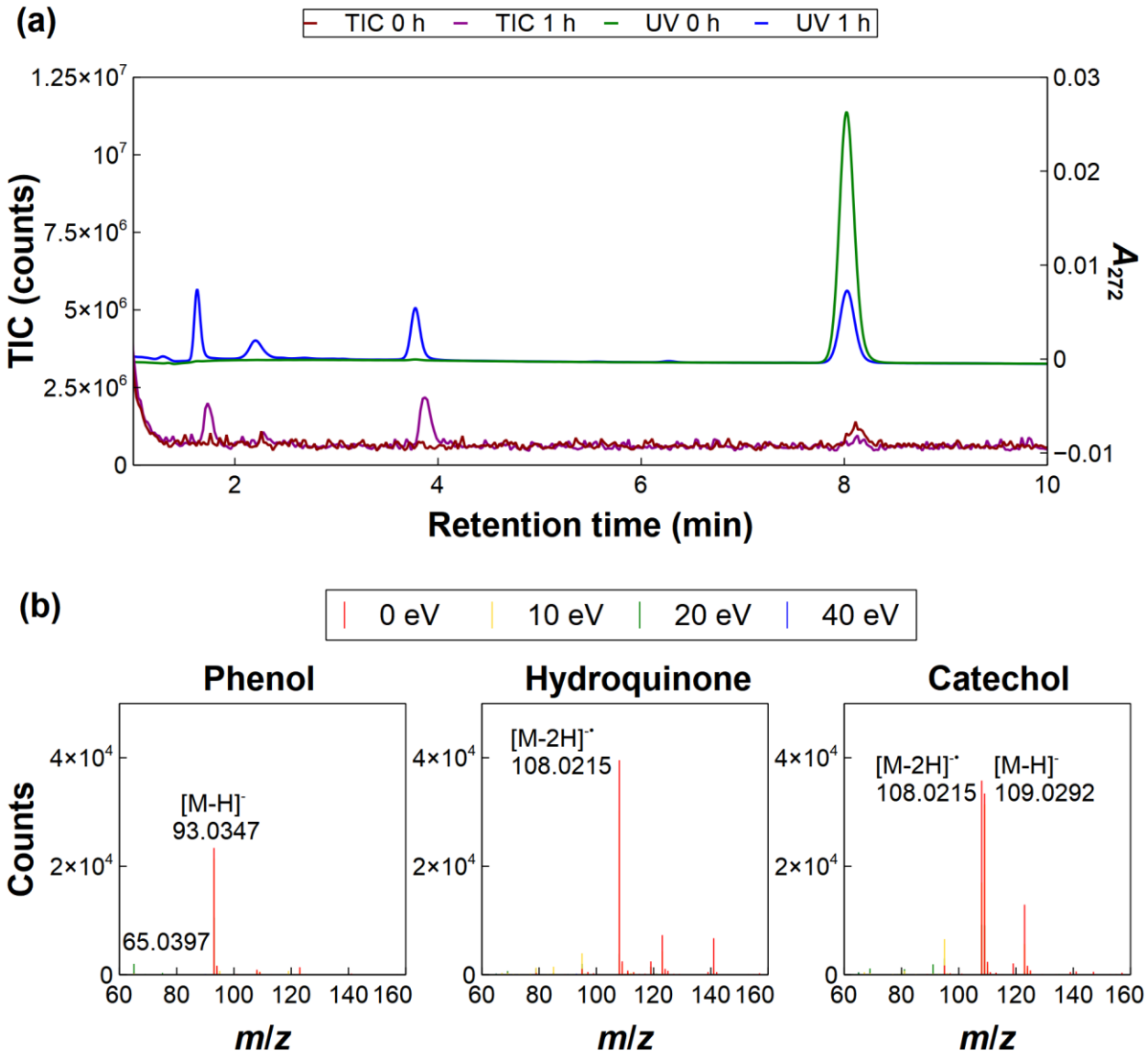

Figure S7. UV and TIC chromatograms for 20 mg L^{-1} phenol samples after 0 h and 1 h irradiation using 100 mg L^{-1} of bare TiO_2 NPs (a), and mass spectra for phenol, hydroquinone, and catechol identified in the samples (b).

Additional phenol degradation experiments

Total organic carbon (TOC) measurements were conducted to evaluate overall mineralization in the photodegradation of 50 mg L^{-1} phenol. The initial concentration of TOC measured across the three samples was 37.2 ± 0.4 (mg C) L^{-1}, which is close to the theoretical value of 38.3 (mg C) L^{-1} for 50 mg L^{-1} of phenol. The percent TOC removal was then computed using the final TOC measured after 300 min of irradiation (Figure S8).

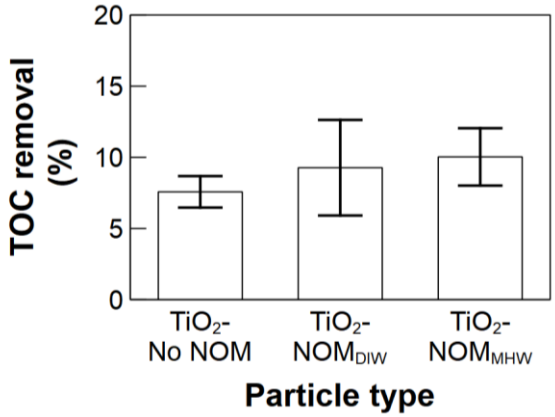

Figure S8. TOC removal in 50 mg L^{-1} phenol degradation after 300 min of irradiation using 100 mg L^{-1} of TiO_2-No NOM, TiO_2-NOM_{DIW}, or TiO_2-NOM_{MHW} (all in 10 mM phosphate buffer). Error bars represent standard deviation across duplicate experiments.

A mole balance was computed for the phenol, hydroquinone, and catechol as measured by LC with UV detection. Despite the differences in catechol observed across the three samples, the overall mole balance was similar across the different TiO_2 NPs, given the lower molar concentrations of catechol relative to the phenol and hydroquinone (Figure S9). Comparing the molar concentrations of the three measured compounds after 300 min to the TOC removal suggests that additional byproducts besides hydroquinone and catechol are present in the samples that are measured by TOC but were not quantified in the LC analysis.

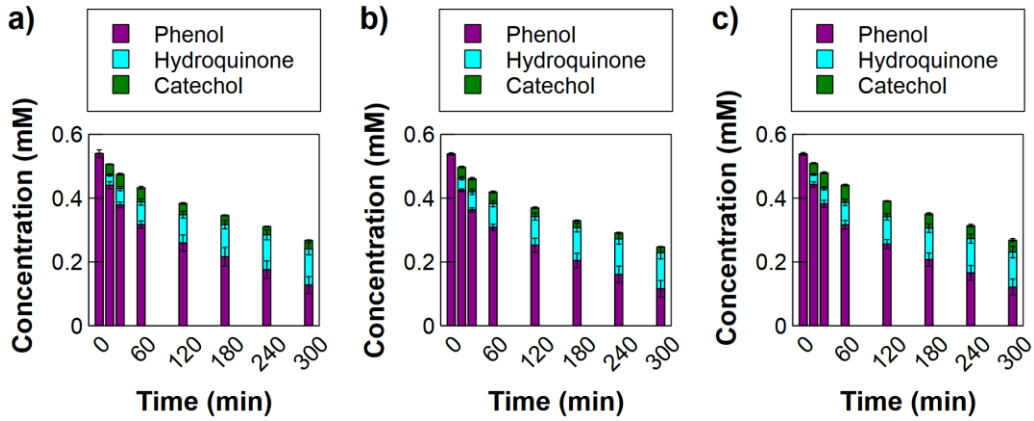

Figure S9. Mole balance for 50 mg L^{-1} phenol degradation after 300 min of irradiation using 100 mg L^{-1} of TiO_2-No NOM (a), TiO_2-NOM_{DIW} (b), or TiO_2-NOM_{MHW} (c) (all in 10 mM phosphate buffer). Error bars represent standard deviation across triplicate experiments.

To evaluate any possible influence of adsorbed bicarbonate from the MHW, phenol degradation experiments were conducted on bicarbonate-exposed TiO_2 samples transferred into 10 mM phosphate buffer (Figure S10). No significant differences were observed for any species (phenol, hydroquinone, catechol) relative to the TiO_2-No NOM.

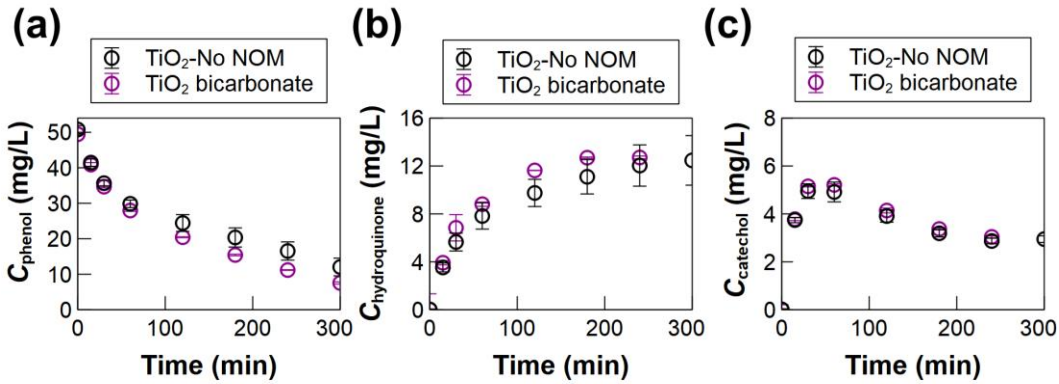

Figure S10. Degradation of 50 mg L^{-1} phenol (a), formation and/or degradation of hydroquinone (b) and catechol (c) using 100 mg L^{-1} of TiO_2-No NOM, or TiO_2 in 1.2 mM $NaHCO_3$. Error bars represent standard deviation across duplicate experiments.

Degradation of pure catechol by the bare and NOM-coated TiO_2 NPs

The phosphate-treated NPs were tested for direct degradation of pure catechol (20 mg L^{-1}) (Figure S11). The lack of significant difference suggests that other species (including phenol, hydroquinone, and other byproducts) may outcompete catechol for reactive oxygen species to exacerbate differences in the phenol degradation experiments.

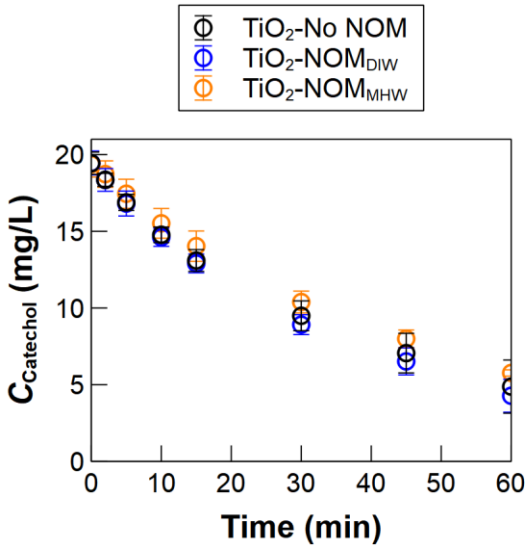

Figure S11. Degradation of 20 mg L^{-1} catechol using 100 mg L^{-1} of TiO_2-No NOM, TiO_2-NOM_{DIW}, or TiO_2-NOM_{MHW} (all in 10 mM phosphate buffer). The experiment was carried out in triplicates.

Singlet oxygen probe experiments

Photoreactivity experiments were conducted using furfuryl alcohol as a probe compound for singlet oxygen and showed no difference in singlet oxygen generation among the three TiO_2 NP samples (Figure S12).

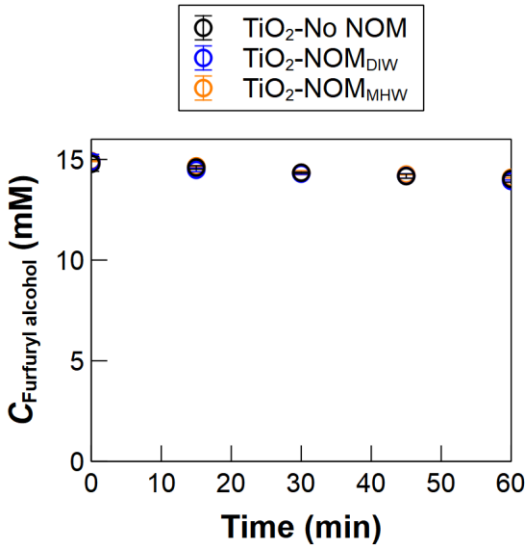

Figure S12. Singlet oxygen generation monitored by degradation of 15 mM furfuryl alcohol as a probe compound using 100 mg L^{-1} of TiO_2-No NOM, TiO_2-NOM_{DIW}, or TiO_2-NOM_{MHW} (all in 10 mM phosphate buffer). Error bars represent the standard deviation across duplicate experiments.

Simulation of electron paramagnetic resonance (EPR) spectrum

The EPR spectrum of the UV-irradiated TiO_2-No NOM sample was simulated using two conformers of BMPO-OH adduct (Figure S13).

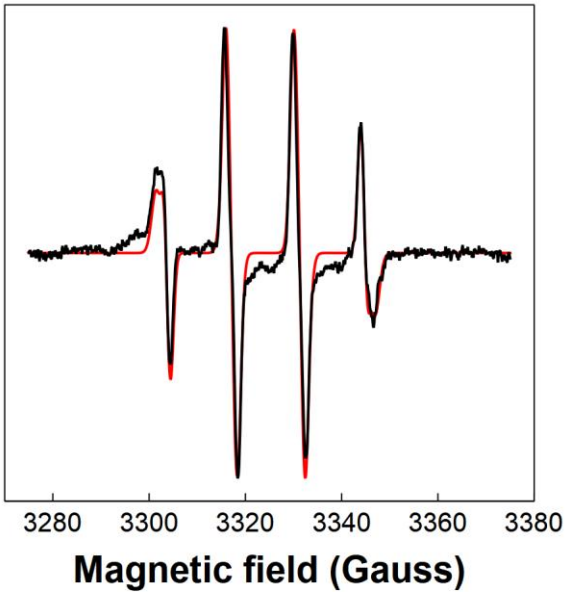

Figure S13. Simulation of the EPR spectrum of the BMPO-OH adduct in UV-irradiation reaction with TiO_2-No NOM. The EPR spectrum (black) is simulated assuming an equilibrium of two conformers (red), A (43%) and B (57%). The parameters for simulation are, (A) g = 2.004, A_N = 14.0 G, $A_{\beta H}$ = 12.8 G, $A_{\gamma H}$ = 0.67 G, and linewidth = 1.3 G; (B) g = 2.004, A_N = 14.33 G, $A_{\beta H}$ = 14.8 G, $A_{\gamma H}$ = 0.8 G, and linewidth = 2.0 G.

References

1. International Humic Substances Society (IHSS), Elemental Compositions and Stable Isotopic Ratios of IHSS Samples, https://humic-substances.org/elemental-compositions-and-stable-isotopic-ratios-of-ihss-samples/, (accessed May, 2021).
2. International Humic Substances Society (IHSS), Acidic Functional Groups of IHSS Samples, https://humic-substances.org/acidic-functional-groups-of-ihss-samples/, (accessed May, 2021).
3. International Humic Substances Society (IHSS), 13C NMR Estimates of Carbon Distribution, https://humic-substances.org/13c-nmr-estimates-of-carbon-distribution-in-ihss-samples/, (accessed May, 2021).
4. P. A. Connor and A. J. McQuillan, Phosphate Adsorption onto TiO_2 from Aqueous Solutions: An in Situ Internal Reflection Infrared Spectroscopic Study, *Langmuir*, 1999, **15**, 2916-2921.
5. F. Bollino, E. Armenia and E. Tranquillo, Zirconia/Hydroxyapatite Composites Synthesized Via Sol-Gel: Influence of Hydroxyapatite Content and Heating on Their Biological Properties, *Materials (Basel)*, 2017, **10**, 757.
6. S. Jayalath, H. Wu, S. C. Larsen and V. H. Grassian, Surface Adsorption of Suwannee River Humic Acid on TiO_2 Nanoparticles: A Study of pH and Particle Size, *Langmuir*, 2018, **34**, 3136-3145.
7. G. B. Deacon and R. J. Phillips, Relationships between the carbon-oxygen stretching frequencies of carboxylato complexes and the type of carboxylate coordination, *Coord. Chem. Rev.*, 1980, **33**, 227-250.

8. C. C. R. Sutton, G. da Silva and G. V. Franks, Modeling the IR Spectra of Aqueous Metal Carboxylate Complexes: Correlation between Bonding Geometry and Stretching Mode Wavenumber Shifts, *Chem. Eur. J.*, 2015, **21**, 6801-6805.

9. S. M. Louie, E. R. Spielman-Sun, M. J. Small, R. D. Tilton and G. V. Lowry, Correlation of the Physicochemical Properties of Natural Organic Matter Samples from Different Sources to Their Effects on Gold Nanoparticle Aggregation in Monovalent Electrolyte, *Environ. Sci. Technol.*, 2015, **49**, 2188-2198.

10. S. M. Louie, R. D. Tilton and G. V. Lowry, Effects of Molecular Weight Distribution and Chemical Properties of Natural Organic Matter on Gold Nanoparticle Aggregation, *Environ. Sci. Technol.*, 2013, **47**, 4245-4254.

11. S. Shakiba, A. Hakimian, L. R. Barco and S. M. Louie, Dynamic Intermolecular Interactions Control Adsorption from Mixtures of Natural Organic Matter and Protein onto Titanium Dioxide Nanoparticles, *Environ. Sci. Technol.*, 2018, **52**, 14158-14168.

12. D. B. Wagoner, R. F. Christman, G. Cauchon and R. Paulson, Molar Mass and Size of Suwannee River Natural Organic Matter Using Multi-Angle Laser Light Scattering, *Environ. Sci. Technol.*, 1997, **31**, 937-941.

13. M. A. Fahmey, M. A. Zayed and Y. H. Keshk, Comparative study on the fragmentation of some simple phenolic compounds using mass spectrometry and thermal analyses, *Thermochim. Acta*, 2001, **366**, 183-188.

14. I. Hassan, J. Pavlov, R. Errabelli and A. B. Attygalle, Oxidative Ionization Under Certain Negative-Ion Mass Spectrometric Conditions, *J. Am. Soc. Mass Spectrom.*, 2017, **28**, 270-277.